REPORT DOCUMENTATION PAGE

Form Approved
OMB No. 0704-0188

PLEASE DO NOT RETURN YOUR FORM TO THE ABOVE ADDRESS.

1. REPORT DATE *(DD-MM-YYYY)*	2. REPORT TYPE	3. DATES COVERED *(From - To)*
16 April 2018	Final	01/01/2013 - 31/12/2017

4. TITLE AND SUBTITLE

Modeling the Influences of Acoustic-Gravity Waves Due to Seismic Events and Atmospheric Sources on the Low- to Mid-Latitude Ionosphere

Final Report

5a. CONTRACT NUMBER

5b. GRANT NUMBER

N00014-13-1-0488

5c. PROGRAM ELEMENT NUMBER

6. AUTHOR(S)

David C. Fritts

5d. PROJECT NUMBER

5e. TASK NUMBER

5f. WORK UNIT NUMBER

7. PERFORMING ORGANIZATION NAME(S) AND ADDRESS(ES)

GATS
11864 Canon Blvd., Suite 101
Newport News, VA 23606

8. PERFORMING ORGANIZATION REPORT NUMBER

9. SPONSORING/MONITORING AGENCY NAME(S) AND ADDRESS(ES)

Office of Naval Research
875 North Randolph Street
Arlington, VA 22203-1995

10. SPONSOR/MONITOR'S ACRONYM(S)

ONR

11. SPONSOR/MONITOR'S REPORT NUMBER(S)

12. DISTRIBUTION/AVAILABILITY STATEMENT

Unlimited

13. SUPPLEMENTARY NOTES

NA

14. ABSTRACT

Numerical simulations of gravity waves (GWs) and acoustic waves (AWs) arising from various sources, and/or propagating in complex environments, have revealed a diversity of responses in the mesosphere, lower thermosphere, and ionosphere (MLTI). Major neutral atmosphere results include 1) large-amplitude GW responses, and tidal modulation, in the TI accompanying tsunami propagation at the ocean surface, 2) strong secondary GW (SGW) and AW forcing due to mountain wave breaking and turbulence in the stratosphere, 3) highly variable GW responses in mesospheric inversion layers (MILs), among them partial transmission and reflection, dissipation and turbulent mixing in the MIL, and confirmation of predictions of a turbulent Prandtl number Pr>1 and energy dissipation rates inferred from vertical velocity variances, and 4) large-scale SGWs arising from local body forcing for 3D GW packets. Ionospheric responses included 1) equatorial plasma bubble (EPB) responses to localized GW packets, 2) "valley region" echoes at low latitudes, and 3) surprising mid-latitude spread F echoes, including indications of "top-side" turbulence where neither neutral nor ionospheric turbulence sources were believed to be viable.

15. SUBJECT TERMS

gravity waves, secondary gravity waves, wave breaking and turbulence, acoustic waves, acoustic wave sources, ionospheric irregularities, equatorial plasma bubbles, mid-latitude spread F, traveling ionospheric disturbances

16. SECURITY CLASSIFICATION OF:			17. LIMITATION OF ABSTRACT	18. NUMBER OF PAGES	19a. NAME OF RESPONSIBLE PERSON
a. REPORT	b. ABSTRACT	c. THIS PAGE			David C. Fritts
U	U	U	UU	10	19b. TELEPHONE NUMBER *(Include area code)* 720-274-4747

Modeling the Influences of Acoustic-Gravity Waves Due to Seismic Events and Atmospheric Sources on the Low- to Mid-Latitude Ionosphere
- Final Report (Period of Performance – 1 June 2013 to 31 December 2017)

David C. Fritts
GATS/Boulder, 3360 Mitchell Lane, Boulder CO 80301
phone: (720) 274-4747 fax: (720) 305-4457 email: dave@gats-inc.com

Contract Number: N00014-13-1-0488

Date: 16 April 2018

LONG-TERM GOALS

The goals of our research within the ONR BRC program were to advance the understanding of, and predictive capabilities for, forcing of the ionosphere accoumpanying acoustic-gravity waves arising due to terrestrial and atmospheric sources.

OBJECTIVES

Our four-year research program was a collaborative effort between GATS, which employs a finite-volume (**FV**) code to describe the nonlinear dynamics of acoustic-gravity waves (**AGWs**) in a deep atmosphere, and the Naval Research Lab. (**NRL**), which developed the SAMI3/ESF model of the ionosphere. Employing the FV code results as inputs to the SAMI3/ESF global ionosphere model enabled us to jointly address ionospheric responses to various anticipated AGW sources, parameters, and spatial distributions. Our specific research objectives addressed included the following:

1. ***Apply coupled neutral atmosphere and ionosphere models to atmospheric AGW sources and their ionospheric responses*** to address the effects of these dynamics, and their responses to various environmental conditions,
2. ***Define AGW responses from the surface into the thermosphere for idealized seismic and atmospheric sources and propagation environments***, including all relevant physical processes, i.e., 1-, 2-, and 3-dimensional (**1D**, **2D**, and **3D**) sources and propagation, transience, nonlinearity, and AGW saturation processes),
3. ***Determine the ionospheric responses to AGWs from various seismic and atmospheric sources and their dependence on atmospheric and ionospheric parameters*** via coupling of our neutral and ionospheric models and evaluation/validation of model results where ionospheric responses were characterized by observations for representative AGWs.

Efforts have addressed mesospheric, thermospheric, and ionospheric responses to AGW having representative amplitudes, scales, and frequencies based on observations throughout the lower and middle atmosphere. These dynamics included propagation of 1D, 2D, and 3D AGWs in variable environments, effects of transience, nonlinearity, 2D and 3D instability dynamics and turbulence, and their plasma responses in the ionosphere. Applications to tsunami-driven AGW responses due to peak ocean surface displacements of ~0.5 m, wavelengths of ~100-400 km, and phase speeds of 200 m/s employed representative thermospheric temperature and tidal wind fields. Applications of these results in the NRL SAMI3/ESF and the Cornell ionospheric models were employed to explore the ionospheric responses to these neutral forcing conditions.

APPROACH

We have employed both anelastic and compressible FV codes, the NRL SAMI3/ESF global ionosphere model, and the Cornell electrodynamics code for our collaborative studies. The FV codes were developed specifically for deep AGW dynamics studies and solve the anelastic or compressible Navier-Stokes equations in 2D or 3D. The FV codes can employ idealized or realistic AGW forcing at the Earth's surface, or at intermediate altitudes as needed, to describe various sources and the AGW spatial and temporal distributions that arise from them. The compressible FV code has also recently been modified to allow stretched grids that enable very high resolution in small portions of much larger domains for cases in which instability dynamics are spatially confined. Suitable FV code output fields are employed as neutral seeds for the longitudinal wedge within the NRL SAMI3/ESF code. The SAMI3/ESF code was developed at NRL to address ionospheric dynamics extending to very small spatial scales. Similar capabilities extending to even smaller scales are provided by the Cornell electrodynamics code employed for several of the applications explored here. Together, these codes offered unique capabilities for addressing AGW responses in the ionosphere. Because the responses to the various dynamics considered here include both gravity wave and acoustic wave responses, we will refer to these separately as GWs and AWs hereafter, as appropriate.

INITIAL RESULTS

The GATS portion of this joint research had multiple thrusts. All included suites of simulations addressing atmospheric and tsunami sources of GWs and their penetration to, and dynamics in, the mesosphere and thermosphere. Parallel plasma simulations employing these neutral dynamics as seeding conditions were explored by colleagues at NRL and Cornell University. Below, we summarize the results of these efforts, seveal of which are ongoing.

GW plasma bubble seeding: An early study examined a GW arising from a lower atmosphere source to explore the efficiency of equatorial plasma bubble (**EPB**) seeding due to differing GW phase alignments in the two hemispheres at the seeding altitudes. The initial conditions are shown in **Figure 1** (top). The left and right panels at bottom show two cases with aligned and anti-aligned GW fields at the two ends of the field lines. Alignment was found to enable much more efficient EPB seeding (see *Wu et al.*, 2015).

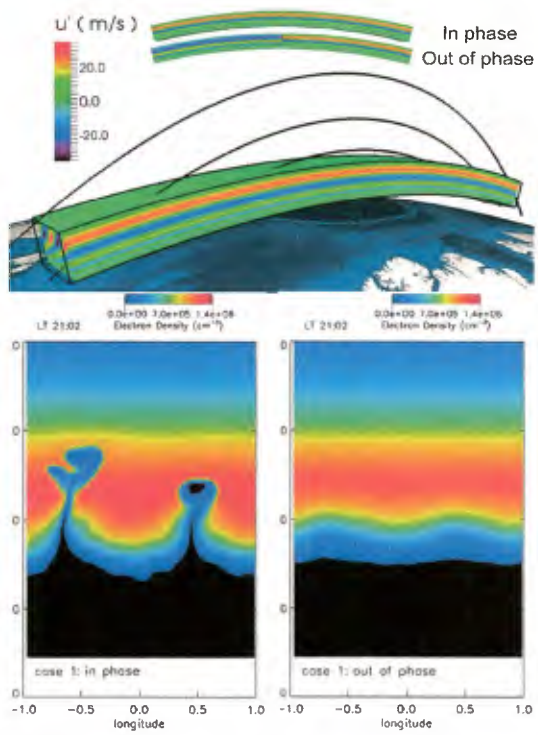

Figure 1. GW seeding conditions and EPB structures (top and bottom) generated by SAMI3/ESF with a GW seed with λ_h=120 km (*Wu et al.*, 2015).

GW self-acceleration dynamics: A second suite of simulations using the anelastic FV code continued a series begun previously addressing self-acceleration (SA) dynamics for GW packets localized in one, two, and three spatial dimensions. GW packets localized only in altitude exhibit strong mean-flow accelerations and GW phase distortions that ultimately cause their dissipation. These SA dynamics are illustrated for one case in the u', w', vorticity, and T' fields at three times in **Figure 2**, and described more completely by *Fritts et al.* (2015). Newer results have expanded the

initial studies for initial GW packets localized in 2D and 3D. These show similar SA dynamics, but also represent a very strong source for secondary GWs and AWs at larger spatial scales that readily penetrate much higher into the thermosphere. An example of these dynamics using the anelastic FV code in 2D is shown at 5 times following the initial linear forcing in **Figure 3**. Note the much larger GW scales and penetration altitudes in the latter three panels. This series of simulations expanded with newer simulations addressing 3D packet responses (see below), and a second SA paper describing these results is in preparation (*Fritts et al.*, 2018a).

Tsunami GW forcing and responses in variable tidal fields: We have performed a suite of anelastic FV code simulations addressing GW responses to tsunamis. Initial studies employed tsunami packets having multiple scales and varying tidal fields extending into the thermosphere. Performing such simulations in a deep domain was critical to providing adequate initial conditions for initiation of tsunami forcing of ionospheric responses in the SAMI3/ESF model, given the potential for an elevated F layer under moderate and strong solar forcing conditions. Thus we used a thermospheric temperature profile that approaches ~800 K at higher altitudes (e.g., solar mean conditions) and canonical winds approximating tidal forcing of 100-150 m/s larger and smaller than the surface wind in the direction of the tsunami propagation direction. These profiles are illustrated in **Figure 4**. The assumed surface displacement and induced vertical velocity for these initial cases using a tsunami phase speed of 200 m/s are shown in **Figure 5**.

The multiple cases explored yielded a range of responses, among them 1) confinement of peak amplitudes to lower altitudes (~200 km) when thermospheric tailwinds are strong, 2) refraction to larger vertical scales, amplitudes, and higher

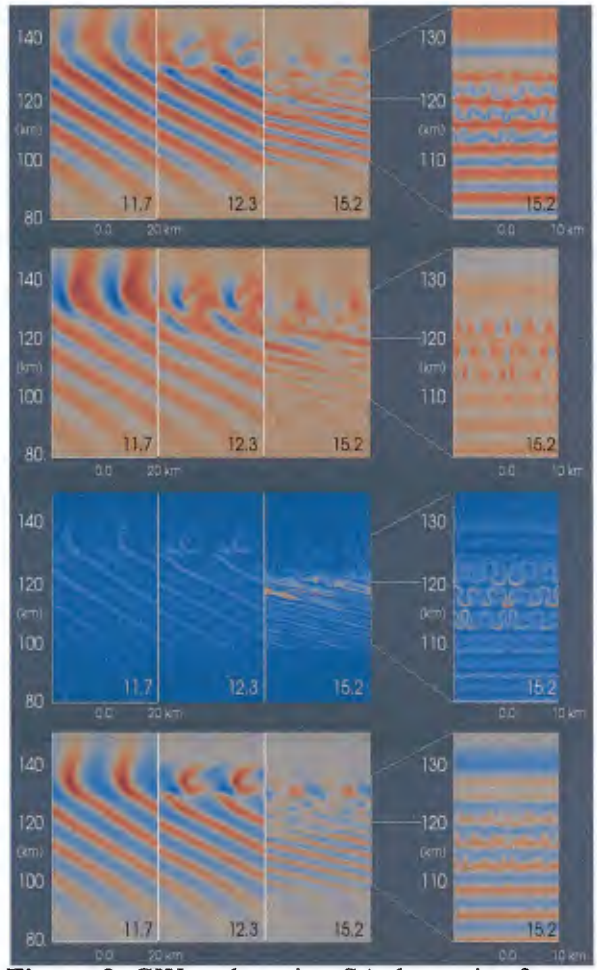

Figure 2. GW undergoing SA dynamics for a packet localized only in altitude with $\lambda_h = \lambda_z =$ 20 km and $\omega_i = N/1.4$.

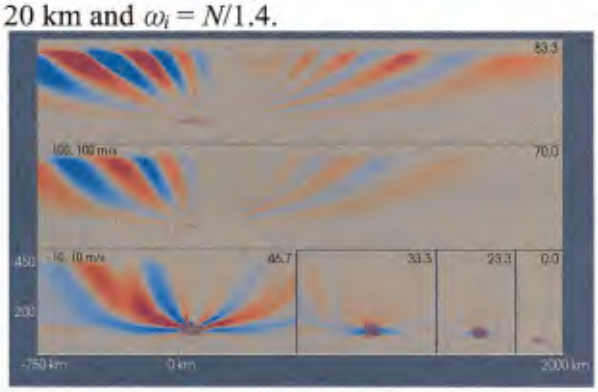

Figure 3. GW and mean perturbation u (positive, red, to the right) due to a 2D Gaussian GW packet having $\lambda_h = \lambda_z = 20$ km and $\omega_i = N/1.4$ propagating to the left at the times shown (in minutes). The domain is 1000x450 km. Secondary GWs having large λ_h, λ_z, and phase speeds arise accompanying accelerating local mean flows (blue, to the left) due to SA dynamics as the GW reaches higher altitudes.

altitudes (300 km) when thermospheric headwinds are strong, 3) significant amplitude attenuation when large tides at lower altitudes lead to turning levels, 4) the large-wavelength components always penetrate to higher altitudes, and 4) nonlinear effects for deeper propagation lead to phase distortions and SA dynamics. Two examples of these evolutions are shown comparing headwinds and tailwinds with and without tidal structures at left and right in **Figure 6**. These results were described in a paper by *Laughman et al.* (2017).

MORE RECENT RESULTS

Our various FV code simulation suites have revealed a number of key dynamics that impact how, and the conditions under which, initial GWs and secondary GWs and AWs impact the mesosphere, thermosphere, and ionosphere (MTI). AGWs from multiple sources readily propagate into the TI, but their roles vary and their responses depend on their scales, amplitudes, and the altitudes to which they propagate. Nonlinear dynamics are expected to play major roles in preventing, or altering, AGW penetration to very high altitudes. These occur when AGW amplitudes become large, and there are various dynamics that can cause large amplitudes at large vertical scales.

Self-acceleration dynamics in 2D & 3D

SA dynamics also operate for AGW packets localized in 3D, and yield a generalization of the results seen to occur for 1D and 2D AGW packets. Because the

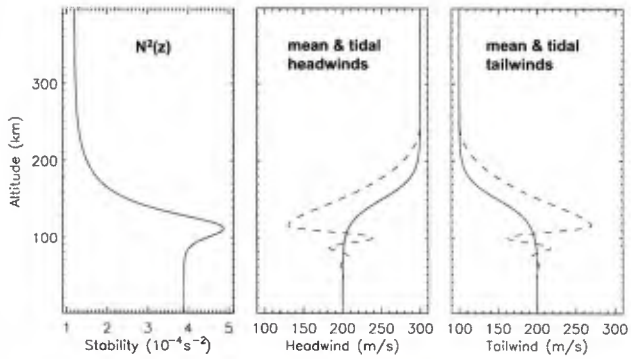

Figure 4. Background atmospheric stability, $N^2(z)$ and headwind and tailwind profiles employed for our recent tsunami AGW forcing cases.

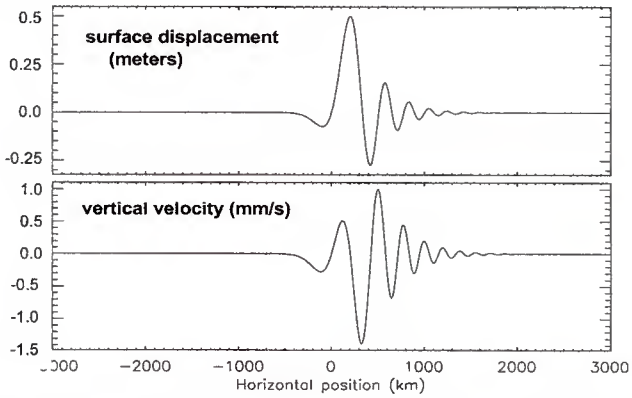

Figure 5. Surface displacement and vertical velocity for a tsunami phase speed of 200 m/s employed for our AGW response simulations.

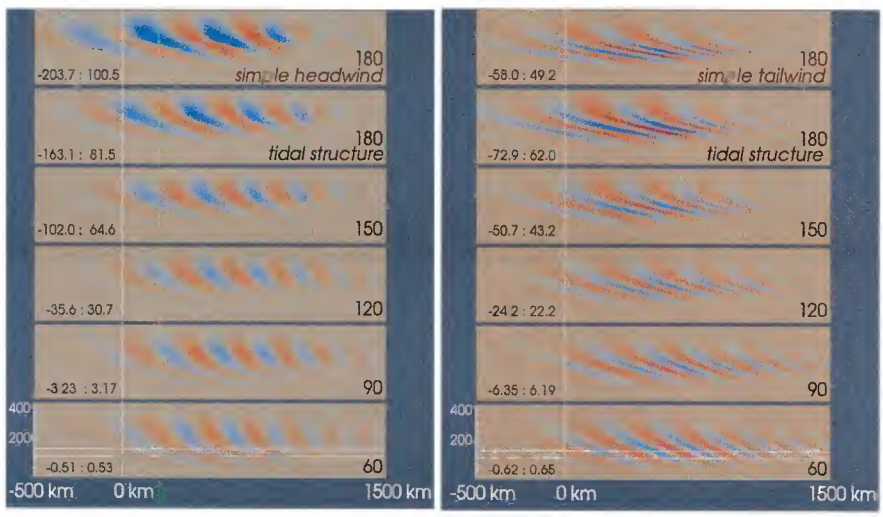

Figure 6. Tsunami responses in u' for the forcing and environment shown in Figure 4 and 5 and a 100 m/s TI headwind (left). As at left, but for mean and tidal tailwinds of 100 m/s in the thermosphere. Min/max velocities and image times (in min) are at left and right.

momentum transported by the AGW is confined in 3D, it yields transient accelerations also confined in 3D. This causes a local roughly Gaussian forcing of the mean flow (and an associated vertical circulation) and advection of the AGW phase structure. The advected phase structures are shown in U at two times in **Figure 7**; the AGW field at higher altitudes arising due to the localized forcing is shown in the T' and U fields as vertical cross sections in **Figure 8**. As seen for the AGW packet localized in 2D (Figure 3), these SA dynamics excite secondary AGWs having much larger horizontal and vertical scales that readily penetrate to higher altitudes (see the left and right edges of the panels in Figure 8). These results will be described in a second paper on these SA dynamics by *Fritts et al.* (2018a).

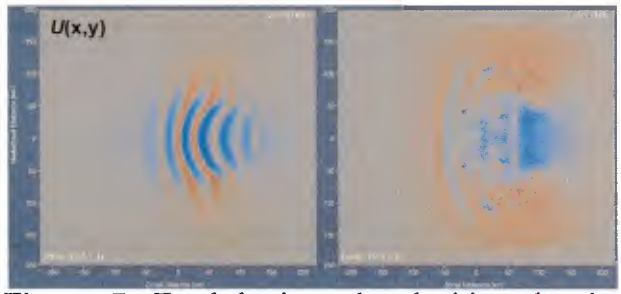

Figure 7. Total horizontal velocities showing AGW SA dynamics in a horizontal plane at 12.5 and 19.3 T_b after initiation of the AGW packet. AGW propagation and mean flow accelerations are towards the left.

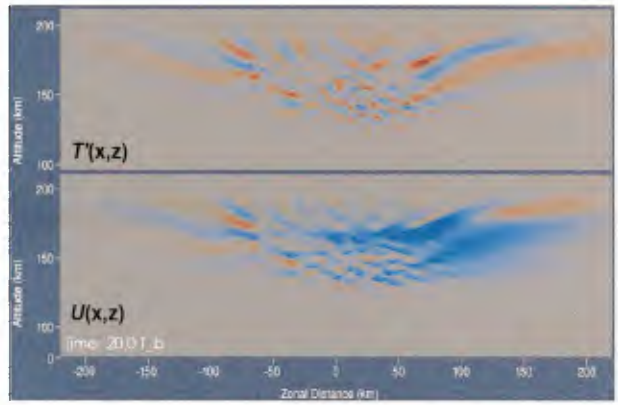

Figure 8. As in Figure 7 for T' and U in vertical planes through the center of the AGW packet along the direction of AGW propagation at 20 T_b.

AGW instabilities due to variable $N^2(z)$

We completed a series of simulations addressing GW propagation, reflection, trapping, and induced instabilities in variable stratification profiles, given the evidence for such features throughout the atmosphere. Initial efforts focused on the dynamics accompanying an AGW encountering an idealized mesospheric inversion layer (**MIL**) comprising a region of higher stratification centered at 75 km beneath a layer having a minimum stability N^2=0 at 85 km, with the maximum and minimum N^2 separated by ~10 km.

Two MIL cases at small and large amplitudes are compared with the same AGW packet without a MIL in **Figure 9**. The linear MIL case (center) exhibits partial reflection and transmission; the nonlinear case (right) exhibits strong trapping, hence strong amplitude increases in the MIL, instabilities and breaking, and strongly suppressed transmission and reflection due to dissipation in the MIL. The initial instabilities driving the transition to turbulence are described well and shown in **Figure 10**. These exhibit longitudinal instabilities at the strongly-sheared interfaces within the large-amplitude trapped AGW in the MIL.

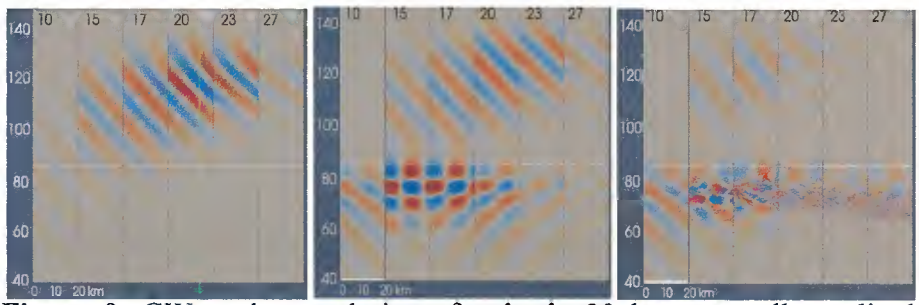

Figure 9. GW packet evolutions for λ_x=λ_z=20 km at small amplitude without an inversion, at small amplitude with an inversion, and at large amplitude with an inversion (left to right) (*Fritts et al.*, 2018b). Times are in T_b.

Turbulence intensities arising from instabilities for two cases having horizontal wavelengths of 20 km and initial vertical wavelengths of 20 and 40 km, respectively, is relatively strong, but spatially localized, with maxima extending ~3 T_b and weaker and variable responses extending another ~10 T_b in each case. The streamwise wavenumber spectra in each case exhibit a roughly -3 slope at low wavenumbers, a $k^{-5/3}$ inertial range at intermediate wavenumbers, and a roll-off into the viscous range at the smallest resolved scales (see **Figure 11**). The subsequent turbulence decay in each case requires another ~10 T_b.

We have also assessed the 2D and 3D (spanwise wavenumbers l=0 and l ≠ 0) momentum and heat fluxes and their influences on the background environment accompanying both evolutions. The mean wind evolutions and 2D and 3D momentum fluxes are shown at left and right for the two cases in **Figure 12**.

The evolving mean winds at top for the 20- and 40-km initial vertical wavelengths (left and right, respectively) reveal the formation of significant induced jets within the MIL having depths of ~3 km in each case.

Corresponding 2D and 3D momentum fluxes (2nd and 3rd rows in Figure 13) reveal that, for these MIL dynamics at least, the 2D GW fluxes are significantly

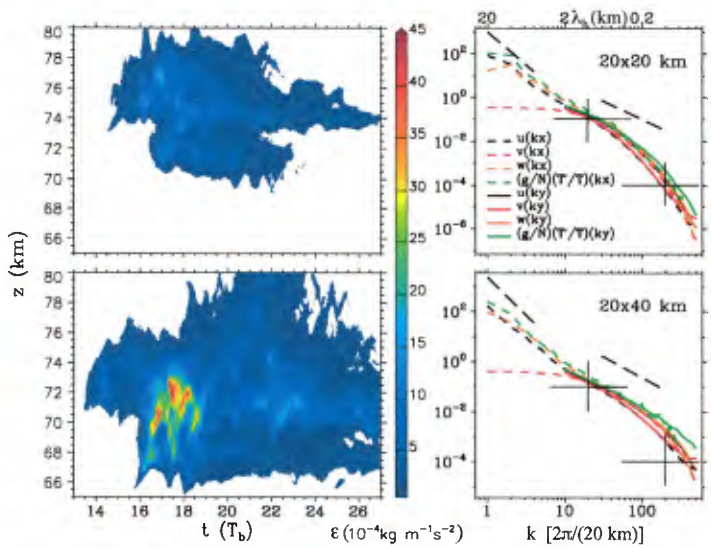

Figure 11. Turbulence energy dissipation rates, ε, at left and streamwise kinetic energy spectra, E(k), at right for the 20- and 40-km initial vertical wavelengths (top and bottom). Dashed lines show -3 and -5/3 spectral slopes and cross hairs are at the same spectral densities for comparison (see Fritts et al., 2018c).

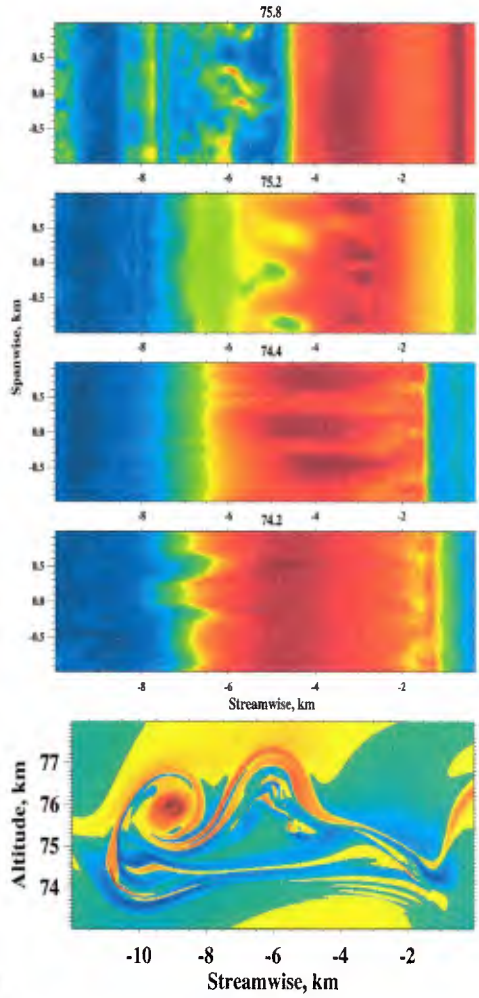

Figure 10. Initial 3D instability structures in the 3rd case shown in Figure 9. The upper four panels show horizontal cross sections at higher to lower altitudes; the lower panel shows a streamwise-vertical cross section spanning the initial instability structures at this time (after *Fritts et al.*, 2018c). Times are in T_b.

larger than the 3D turbulence fluxes (by ~10-30 times). The 2D fluxes also exhibit fluctuations at time scales longer than the GW periods during the transient creation of the jets and at higher frequencies thereafter. Finally, the ratio of heat and momentum fluxes suggest a turbulent Prandtl number Pr ~2-3.

These results are discussed in detail by *Fritts et al.*, 2018b, c).

Neutral atmosphere and ionosphere responses to GW instabilities and GW-tidal interactions in the mesosphere, lower thermosphere, and ionosphere (MLTI)

More recent studies of the influences of GW interactions with tidal fields and their instabilities on the neutral atmosphere and ionosphere at low, middle, and high latitudes have employed the anelastic and compressible FV codes.

a. Equatorial ionospheric "valley waves"

At equatorial latitudes, these dynamics were found to provide a plausible explanation for equatorial "valley waves" seen at Jicamarca, which have been frequently observed, but which have remained unexplained for decades (e.g., *Hysell et al.*, 2017; see **Figures 13 and 14**).

b. Mid-latitude spread F

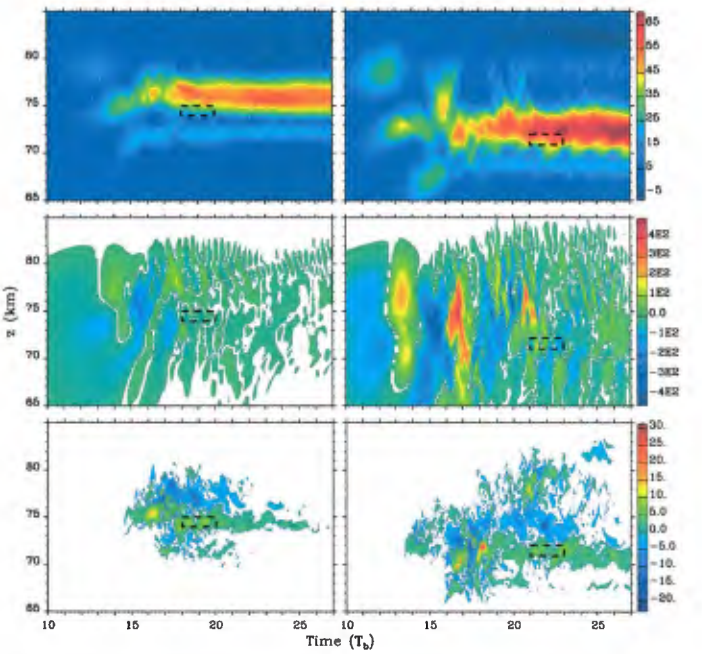

Figure 12. Evolving mean winds in the direction of AGW propagation (top) and 2D and 3D momentum fluxes, <u'w'> (middle and bottom), for the 20- and 40-km initial vertical wavelengths (left and right).

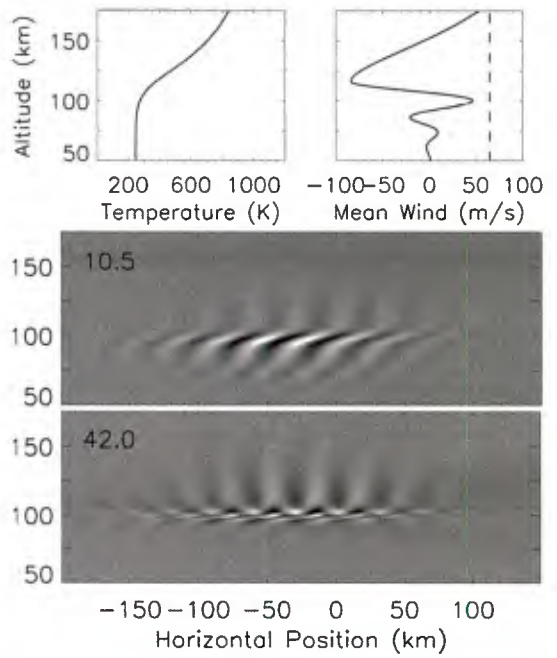

Figure 13. Initial neutral atmosphere $T(z)$ and zonal wind $U(z)$ (at top) and evolving $u'(x,y)$ (middle and bottom) spanning 31.5 min seeding the Cornell electrodynamics model.

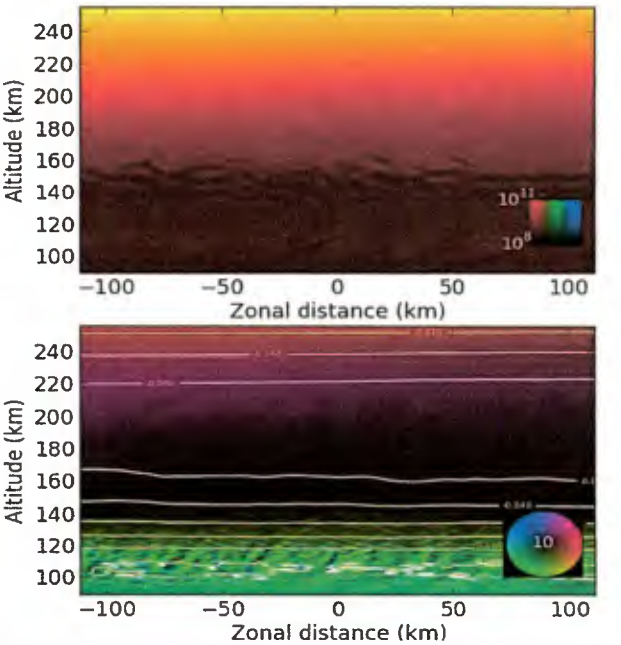

Figure 14. Cornell electrodynamics model plasma density and composition (top) and current density (bottom) in response to the neutral forcing in Figure 13. Red, green, and blue hues denote molecular ions, atomic ions, and protons, respectively.

Similarly, an initial application of neutral seeding of the mid-latitude ionosphere yielded a predicted ionospheric response that closely resembles mid-latitude spread F (see **Figure 15**), for which an explanation had also remained elusive (e.g., *Hysell et al.*, 2017b).

Common features include 1) slanted electron density plumes extending to ~300 km or above, 2) occurrence of the plumes at significant upward displacements of the large-scale electron density fluctuations, and 3) indications of turbulence-like features at higher altitudes where neither the neutral atmosphere nor the ionosphere should be able to generate turbulence.

c. Mountain wave instability dynamics impacting the thermosphere and ionosphere

An application of the new compressible FV code to mountain wave (MW) – tidal interactions for realistic forcing over real 3D terrain was performed using very high resolution where needed to resolve MW breaking dynamics in tidal wind shears at ~80-100 km. This revealed the generation of expected secondary GWs and also unexpected strong AWs having acoustic velocities, large scales, periods of ~2-3 min, and readily attaining much higher altitudes (*Fritts et al.*, 2018d, e, f). Examples of these dynamics are shown in various fields ~1 hr after AGW – tidal interactions began in **Figure 16**.

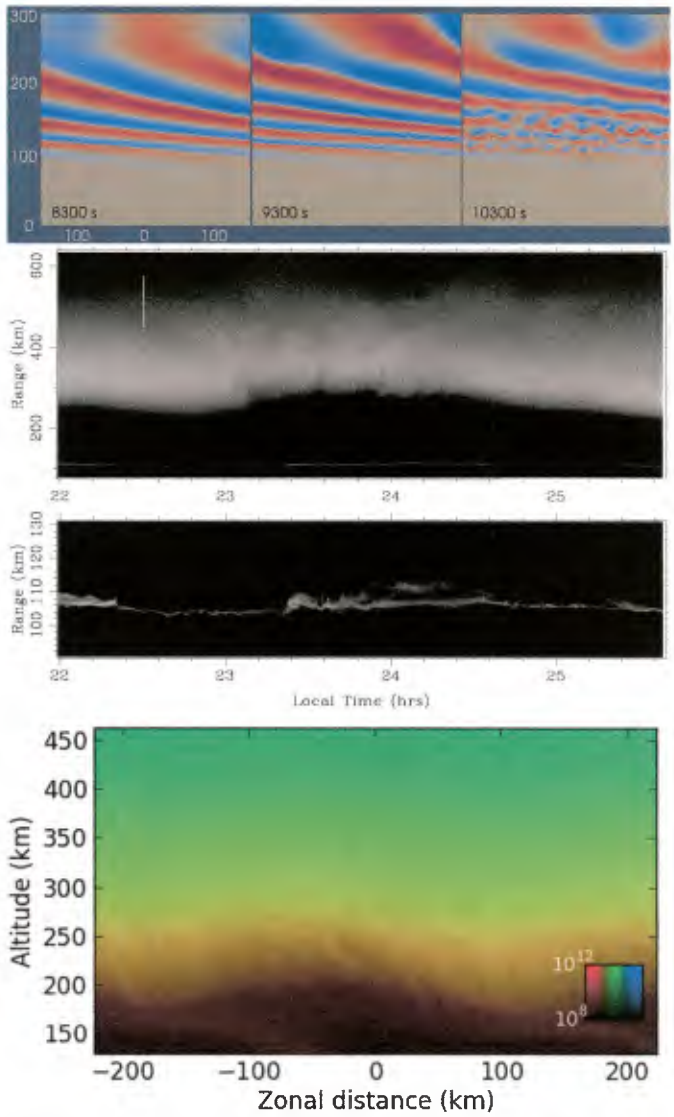

Figure 15. Neutral GW evolution in the lower thermosphere enabling development of large-scale Kelvin-Helmholtz instabilities (top), electron density fluctuations from 90 to 600 km and an expanded view of an apparent traveling ionospheric disturbance (TID) at ~107 km at the lower edge of the upper panel (middle), and electron densities predicted by the Cornell electrodynamics code.

IMPACTS/APPLICATIONS

Our tsunami and more general AGW studies have revealed the potential for GWs and AWs from multiple sources to have influences extending far into the thermosphere, but with strong modulation by tidal fields at the higher altitudes. Such modulation will surely have strong influences on AGW structure and thermospheric and ionospheric responses at multiple scales. Secondary GW and AW generation, in particular, is likely to have strong responses at high altitudes, given their often large spatial scales and phase speeds. The MW simulation has also highlighted the expectation that AWs can be generated by GW breaking and likely have their own influences in the thermosphere and ionosphere.

Our various simulations suggest the possibility for both deterministic and stochastic specifications of AGW influences on plasma dynamics at high altitudes in regions of strong AGW sources. Due to expected strong secondary AGW generation, these hotspot influences should easily extend well into the TI.

Simulations of ionospheric responses that appear to provide explanations for previously unexplained ionospheric observations suggest that other AGW dynamics in the MLT may also induce other ionospheric responses extending to high altitudes.

These new findings are strong motivations to expand our exploration of such neutral atmosphere – ionosphere interactions in future studies.

RELATED PROJECTS

Dave Fritts participated in a NASA project with Dave Hysell at Cornell University for numerical simulations of GWs and their potential plasma influences extending to high altitudes. Dave, Brian Laughman, and Ling Wang also participated in an NSF project that addressed deep GW dynamics related to the NSF/NCAR DEEPWAVE field program performed in New Zealand in 2014. Additionally, Joe Huba at NRL is a Co-PI with Dave on this ONR/BRC project.

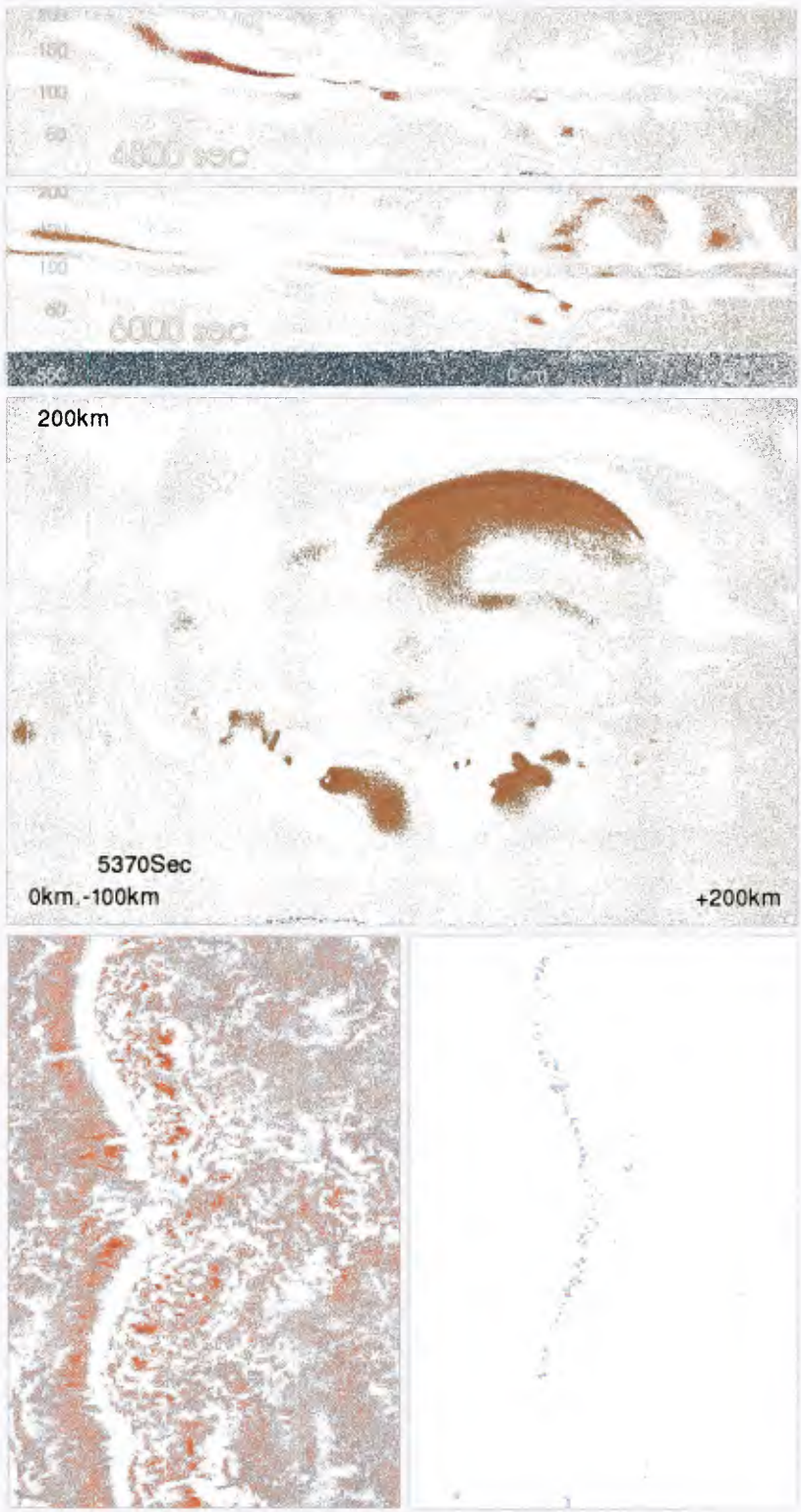

Figure 16. Andes simulation fields showing $u(x,z)$ at 20 and 40 min after the full forcing is achieved (top 2 panels), $w(x,z)$ in a 300-km zonal subdomain (3rd panel), and $T'(x,y)$ and vorticity magnitude, $|\zeta'|(x,y)$, in subdomains 1 hr after full forcing is achieved. Note the very large AWs in the 2nd and 3rd panels.

PUBLICATIONS ARISING FROM THIS ONR ESEARCH SUPPORT

Fritts, D. C., B. Laughman, T. Lund, and J. Snively, 2015: Self acceleration and instability of gravity wave packets, I: Effects accompanying temporal localization, J. Geophys. Res., 120, 8783–8803, doi:10.1002/2015JD023363.

Fritts, D. C., B. Laughman, and T. Lund, 2018a: Self acceleration and instability of gravity wave packets, II: Dynamics of two- & three-dimensional packets, J. Geophys. Res., in preparation.

Fritts, D. C., B. Laughman, L. Wang, T. Lund, and R. L. Collins, 2018b: Gravity Wave Dynamics in a Mesospheric Inversion Layer: 1. Reflection, Trapping, and Instability Dynamics, J. Geophys. Res.: Atmospheres, 123. https://doi.org/10.1002/2017JD027440.

Fritts, D. C., T. S. Lund, B. Laughman, and H.-L. Liu, 2018d: Numerical simulation of mountain waves over the southern Andes, Part 1: Mountain wave and secondary wave evolutions, character, and breaking, J. Geophys. Res., in preparation.

Fritts, D. C., T. S. Lund, B. Laughman, and H.-L. Liu, 2018e: Numerical simulation of mountain waves over the southern Andes, Part 2: Momentum fluxes, mean-flow accelerations, and gravity-wave/tidal interactions, in preparation.

Fritts, D. C., T. S. Lund, B. Laughman, and H.-L. Liu, 2018f: Numerical simulation of mountain waves over the southern Andes, Part 3: Instability dynamics and secondary wave sources, in preparation.

Fritts, D. C., L. Wang, B. Laughman, T. Lund, and R. L. Collins, 2018c: Gravity Wave Dynamics in a Mesospheric Inversion Layer: 2. Instabilities, turbulence, fluxes, and mixing, J. Geophys. Res.: Atmospheres, 123. https://doi.org/10.1002/2017JD027442.

Hysell, D. L., R. Jafari, D. C. Fritts, and B. Laughman, 2014: Gravity wave effects on postsunset equatorial F region stability, J. Geophys. Res. Space Physics, 119, 5847–5860, doi:10.1002/2014JA019990.

Hysell, D. L., D. C. Fritts, B. Laughman, and J. Chau, 2017: Gravity wave-induced ionospheric irregularities in the postsunset equatorial valley region, J. Geophys. Res. Space Physics, 122 (11).

Hysell, D. L., M. Larsen, D. C. Fritts, B. Laughman, and M Sulzer, 2018: Anomalous irregularities in the topside ionosphere above Arecibo, Nature Geoscience, submitted.

Laughman, B., D. C. Fritts, and T. S. Lund, 2017: Tsunami-driven gravity waves in the presence of vertically varying background and tidal wind structures, J. Geophys. Res., 122, DOI: 10.1002/2016JD025673.

Wu, T.-W., J. D. Huba, J. Krall, D. C. Fritts, and B. Laughman 2015: Seeding of equatorial spread F by turbulent gravity waves, Geophys. Res. Lett., 42, doi:10.1002/2014GL062348.